CloudSat mission: Performance and early science after the first year of operation

Graeme L. Stephens,[1] Deborah G. Vane,[2] Simone Tanelli,[2] Eastwood Im,[2]
Stephen Durden,[2] Mark Rokey,[2] Don Reinke,[3] Philip Partain,[4] Gerald G. Mace,[5]
Richard Austin,[1] Tristan L'Ecuyer,[1] John Haynes,[1] Matthew Lebsock,[1]
Kentaroh Suzuki,[1] Duane Waliser,[2] Dong Wu,[2] Jen Kay,[6] Andrew Gettelman,[6]
Zhien Wang,[7] and Rojer Marchand[8]

[1] This paper reports on the early mission performance of the radar and other major aspects of the CloudSat mission. The Cloudsat cloud profiling radar (CPR) has been operating since 2 June 2006 and has proven to be remarkably stable since turn-on. A number of products have been developed using these space-borne radar data as principal inputs. Combined with other A-Train sensor data, these new observations offer unique, global views of the vertical structure of clouds and precipitation jointly. Approximately 11% of clouds detected over the global oceans produce precipitation that, in all likelihood, reaches the surface. Warm precipitating clouds are both wetter and composed of larger particles than nonprecipitating clouds. The frequency of precipitation increases significantly with increasing cloud depth, and the increased depth and water path of precipitating clouds leads to increased optical depths and substantially more sunlight reflected from precipitating clouds compared to than nonprecipitating warm clouds. The CloudSat observations also provide an authoritative estimate of global ice water paths. The observed ice water paths are larger than those predicted from most climate models. CloudSat observations also indicate that clouds radiatively heat the global mean atmospheric column (relative to clear skies) by about 10 Wm^{-2}. Although this heating appears to be contributed almost equally by solar and infrared absorption, the latter contribution is shown to vary significantly with latitude being influenced by the predominant cloud structures of the different region in questions.

1. Introduction

[2] The clouds on Earth are fundamental to most aspects of human life. Through production of precipitation, they are essential for delivering and sustaining the supplies of fresh water upon which human life depends. Clouds exert a principal influence on the planet's energy balance and grossly influence the sensitivity of the climate system to climate forcing through their influence on the solar and infrared radiation that enters and leaves the atmosphere [*Stephens*, 2005]. It is also in clouds that latent heat is released by the process of condensation that, in turn, controls the development and evolution of the planet's storm systems.

[3] Many of the key cloud properties relevant to these important issues are, to first order, governed by the vertical structure of clouds. For example, the degree to which clouds radiatively heat or cool the atmosphere, as we show below, depends on the height of the clouds and whether cloud layers are located above or below them. The ability of clouds to produce precipitation and the amount of precipitation produced is directly related to the depths of clouds. The ability of clouds to warm the surface through emission of radiation depends on the height of cloud bases and so, too, is the potential water holding capability of clouds, which grossly affects the amount of sunlight reflected by clouds to space.

[1]Department of Atmospheric Sciences, Colorado State University, Fort Collins, Colorado, USA.
[2]Jet Propulsion Laboratory, California Institute of Technology, Pasadena, California, USA.
[3]CIRA, Colorado State University, Fort Collins, Colorado, USA.
[4]Science Technology Corporation, MetSat, Fort Collins, Colorado, USA.
[5]Department of Meteorology, University of Utah, Salt Lake City, Utah, USA.
[6]National Center for Atmospheric Research, Boulder, Colorado, USA.
[7]Department of Atmospheric Science, University of Wyoming, Laramie, Wyoming, USA.
[8]Joint Institute for the Study of the Atmosphere and Ocean, University of Washington, Seattle, Washington, USA.
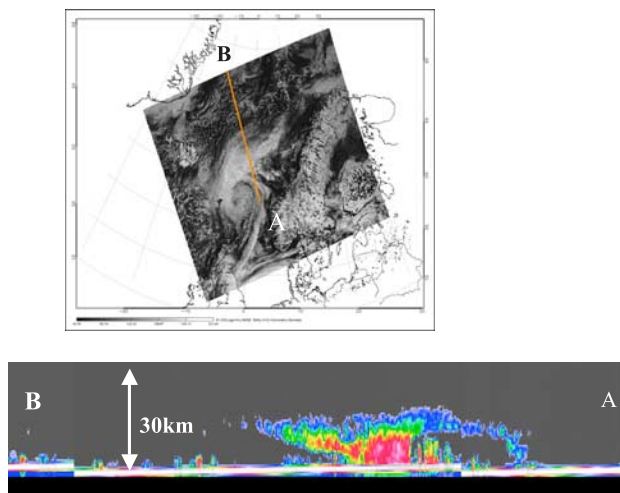
Figure 1. (top) A MODIS image of a warm frontal system intersected by CloudSat along the orbit track highlighted. (bottom) The very first quick-look image of Cloudsat cloud profiling radar (CPR) reflectivity gathered for an approximate 1400 km section of orbit on 20 May 2006, captured immediately after the first turn on of the CPR.

[4] It is for these reasons, among others, that the CloudSat Mission was proposed and selected by NASA as one of three currently operating Earth Systems Science Pathfinder (ESSP) missions. The mission, launched on 28 April 2006, carries the first W-band (94 GHz) cloud profiling radar (CPR) as the only payload instrument. This instrument is unique in its ability to sense condensed cloud particles while coincidently detecting precipitation. The ability to jointly observe clouds and precipitation is beginning to reveal new global insights on the elementary processes by which precipitation forms [e.g., *Stephens and Haynes*, 2007]. Although originally funded to operate for only 22 months, NASA has approved the extension of mission operations to September 2011, contingent on the continuing nominal performance of the instrument. At present, all systems exhibit nominal or better performance and all indicators suggest that an operational life beyond 4–5 years may be possible.

[5] CloudSat was developed as a collaboration between NASA, the Canadian Space Agency (CSA), and the U.S. Air Force. The Jet Propulsion Laboratory (JPL) of the California Institute of Technology developed the payload in partnership with CSA and manages the project for the Principal Investigator at Colorado State University (CSU). CSA contributed key components and subsystems of the radar and has supported sustained validation activities. The U.S. Air Force provides ground operations and manages communications with the spacecraft. The ground operations are performed at the Kirtland Air Force base in Albuquerque, New Mexico. Data are downlinked several times per day through the U.S. Air Force Satellite Control Network (AFSCN) ground receiving stations to the data processing center (DPC) at CSU.

[6] The CPR has been operational since 2 June 2006 and has been acquiring the first-ever, continuous, global time series of vertical cloud structures and properties with 485-m

vertical resolution and 1.4-km antenna 3 dB footprint. Figure 1 presents the historic first-look CPR image of the vertical structure of a warm front over the North Atlantic observed on 20 May 2006. This image was acquired immediately after activation of CPR as part of a brief 4-h checkout test. The richness of the Cloudsat information for studying these classic weather systems has since been highlighted by *Posselt et al.* [2007]. These initial test data were transmitted from the spacecraft to the Kirtland Base ground operations center via one of the SGLS downlink sites, then routed to the DPC at CSU and returned back to Kirtland within 15 min of initial acquisition by the CPR. Near-realtime data of this type are routinely produced as "quick-look" products and are posted typically within 3–10 h on the CloudSat webpage. These timely near-realtime "quick-look" data are currently being exploited in a number of operational applications described elsewhere [*Mitrescu et al.*, 2008].

[7] The purpose of this paper is twofold. The first purpose is to report on the early mission performance of the radar and other major aspects of the mission, including a brief review of the data products now available from the CloudSat data processing center (DPC). The second purpose is to report on new results derived from analysis of these products highlighting progress toward the mission objectives. The four mission objectives are to: (1) quantitatively evaluate the representation of clouds and cloud processes in global atmospheric circulation models, (2) quantitatively evaluate the relationship between the vertical profiles of cloud liquid water and ice and the radiative heating of the atmosphere and surface, (3) evaluate cloud properties retrieved from other satellite systems, in particular those of Aqua, and (4) contribute to improving our understanding of the indirect effect of aerosols on clouds by investigating the effect of aerosols on cloud and precipitation formation.

[8] Details of the formation flying activity and an indication of its performance are described in section 2. Section 3 briefly reviews the CPR and its performance since launch and section 4 describes the various products now available for community use and presents examples of selected products. Results from analysis of these products that contribute to the mission science goals are described in section 5. This discussion is then followed by a summary of the paper in section 6.

2. Formation Flying in the A-Train Constellation

[9] Although the radar measurements alone are of great intrinsic value, the added benefit in combining data sets from other satellite sources was recognized from the outset [*Stephens et al.*, 2002]. Matching the vertical profile information of the radar with other satellite data, for example, provides an opportunity to evaluate cloud products derived from other satellite sensor data as well as the opportunity for developing entirely new information about clouds and precipitation, as exemplified in the results of *Stephens and Haynes* [2007] study. In particular, the synergy between cloud radar and lidar observations, and the anticipated science benefits derived in combining these observations, weighed heavily in the mission design.

[10] A formation-flying element of the mission was thus implemented specifically to enable matching of CloudSat observations closely in time (and space) with the lidar
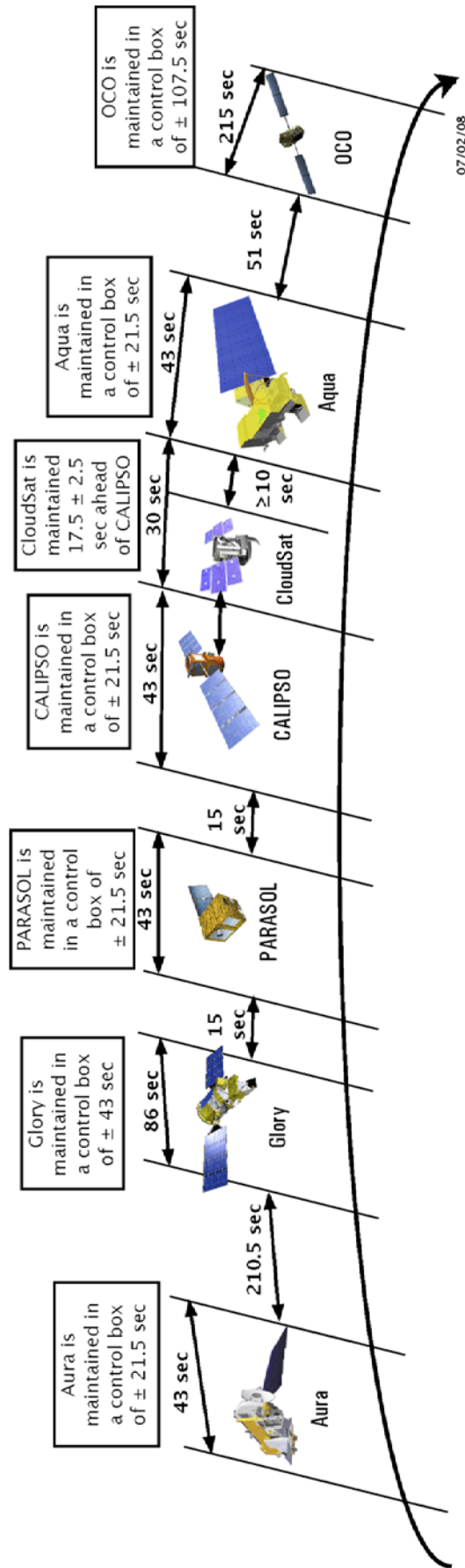
Figure 2. The Afternoon constellation (A-Train) showing in detail the control boxes and the position of each member prior to December 2007. The position of both CloudSat with respect to CALIPSO and Aura with respect to the constellation has been changed (see text).

Table 1. Cloud Profiling Radar Instrument and Performance Parameters

Parameter	Proposed Performance
Frequency	94.05 GHz
Altitude	705–730 km
Range resolution (6 dB)	485 m
Cross-track resolution	1.4 km
Along-track resolution	1.8 km
Pulse width	3.3 μs
Peak power (measured)	32.6 dB
PRF	3700–4300 Hz
Antenna diameter	1.85 m
Antenna gain	63.1 dBi
Antenna sidelobes	−50 dB @ $\theta > 7°$
Integration time (single-beam)	0.16 s
Data window	30 km
Minimum detected reflectivity (measured)	−30 dBZ

observations of CALIPSO [*Winker et al.*, 2007], as well as other more conventional satellite observations. This was achieved by flying CloudSat in the afternoon constellation of satellites (the so-called A-Train constellation [*Stephens et al.*, 2002]). The A-Train is, currently, a five-member constellation of satellites that includes, in addition to the CloudSat and CALIPSO satellites, the EOS Aqua and EOS Aura satellites at each end of the constellation and another small satellite, PARASOL, carrying the POLDER polarimeter [*Deschamps et al.*, 1994] inserted in the formation between Aura and CALIPSO. The orbits of the constellation are Sun-synchronous with a mean equatorial altitude of 705 km and an inclination of 98.2 degrees. This orbit is "frozen" such that there are no long-term period changes in the orbital elements resulting in an orbit of constant size and shape, thus reducing altitude variations over any spot on the Earth and improves the repeatability of scientific observations.

[11] All spacecraft of the Constellation make their routine maneuvers with full knowledge of the operations of other spacecraft coordinated through the Earth Science Missions Office (ESMO) at GSFC. This oversight ensures the overall health and safety of the constellation, ensuring that close approaches that would have an unacceptable probability of collision are avoided. The general approach to managing such risks is based on the concept of the "control box." This is a theoretical construct centered at a reference position on a satellite's drag-free orbit with dimensions defined by an allowable along-track movement relative to the box's center (the reference position). In practice, this along-track movement is coupled with an east–west movement of the satellite's ground track relative to the idealized ground track of the drag-free orbit. It is this limitation in both the along-track and cross-track movements that creates the notion of a "box."

[12] The control boxes of the different members of the constellation are illustrated in Figure 2 where the size of the box is also indicated. For example, the control boxes of both CALIPSO and Aqua are 44 s in size. CloudSat is unique among all members, as its control box lies within the CALIPSO control box and is much more tightly maintained at 5 s in size. This stems from the requirement to place footprints of the radar and lidar within 2 km of each other (across track) 50% of the time. Thus CloudSat is the only spacecraft in the formation that must make frequent, routine

adjustments in its orbit location (called circulation orbits) to maintain the desired spatial overlap of footprints with respect to CALIPSO while maintaining a close proximity with Aqua. As of January 2008, CloudSat has conducted over 40 maneuvers to maintain this formation.

[13] Although the original requirement of the CloudSat formation-flying architecture was to overlay the CPR footprints on the lidar footprints of CALIPSO at least 50% of the time, analysis indicates that this requirement has been substantially exceeded with overlap of CPR and lidar footprints occurring more than 90% of the time. In this way CloudSat has demonstrated that precision formation flying is a practical and viable observing strategy that can be exploited in the design of future Earth observing systems.

[14] In December 2007, the constellation control box separations, as depicted in Figure 2, changed slightly. Aura shifted its position to the east of the idealized reference ground track and moved closer to the other members of the constellation primarily to overlap CloudSat and MLS observations more tightly. CloudSat also moved its control box from 12.5 ± 2.5 s to 17.5 ± 2.5 s with respect to CALIPSO, forced by the CALIPSO change to the pointing of the lidar to 3 degrees off-nadir. The chosen adjustment to the separation of the two satellites attempts to maximize the overlap of the column sampled by the CloudSat radar with the slant column now profiled by CALIPSO.

3. Cloud Profiling Radar

[15] Clouds are weak scatterers of microwave radiation, in contrast to the much stronger reflection from the underlying surface of Earth. The need to detect these weak cloud signals was the overriding requirement on the CPR stated in terms of a minimum detectable cloud reflectivity $Z_{min} \sim$ −28 dBZ (at beginning of life). Although the real desire was to achieve the most sensitive possible radar, the scientific justification and value for the requirement of −28 dBZ is described by *Miller and Stephens* [2001].

[16] This sensitivity requirement forced a number of careful tradeoffs among several competing and often conflicting design parameters as discussed in more detail by *Im et al.* [2005] and *Tanelli et al.* [2008]. The final defining parameters of the radar confirmed by measurement both before and after launch are summarized in Table 1. The major components of the radar hardware that represented some of the technical challenges are illustrated in Figure 3. Two of the more noteworthy components of the radar shown are the high-power amplifier (HPA) subsystem and the antenna subsystem. The HPA, which amplifies the transmitted pulse to a nominal power level of 1.7 kW, consists of an extended interaction klystron (EIK) and a high-voltage power supply (HVPS). The radar uses both a primary and a backup (redundant) HPA to enhance system reliability. The HVPS provides 20 kV needed to operate the EIK. Both the 94-GHz EIK and the 20-kV HVPS on CloudSat are the first of their kinds being flown in space. As of January 2008 it has only been necessary to operate the primary HPA.

[17] The second important component is the antenna subsystem consisting of the collimating antenna and the quasi-optical transmission line (QOTL). The collimating antenna, constructed of composite graphite material, meets the challenge of low surface roughness (less than an RMS of
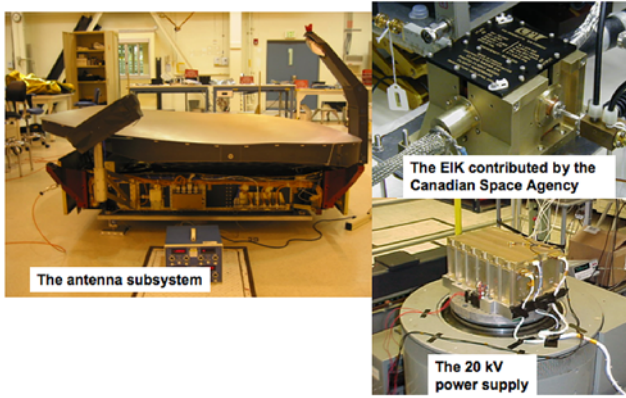
Figure 3. Photographs of three important components of the CPR. The extended interaction klystron and high voltage poser supply integrate to form the High Power Amplifier subsystem.

5 μm over the entire surface) and delivers a highly directional beam of half power full-width < 0.12°. The antenna also has far side lobe levels 50 dB below that of the main lobe as required to remove aliasing of these side lobes into the profiles of the following pulses. Instead of using a conventional waveguide, the antenna is fed by the QOTL for low loss, which is an important consideration in addressing the requirement of minimum sensitivity. The QOTL is also the first time this technology at the millimeter wavelength has flown in space.

3.1. CPR Profile Data

[18] The quantity of immediate relevance is the range-resolved radar cross section per unit volume, η, at a specific range r defined as

$$\eta = \frac{P_{rec}(4\pi)^3 r^2 L_a}{P_t \lambda^2 G_{rec} G^2 \Omega \Delta} \quad (1)$$

where P_{rec} is the output power of the receiver, P_t is the transmitted power, λ is the wavelength, G_{rec} is the receiver gain, G is the antenna gain, r is the range to the atmospheric target, Ω is the integral of the normalized two-way antenna pattern, Δ is the integral of the received waveform shape, and L_a is the two-way atmospheric loss. The quantity η is converted to the equivalent (attenuated) range-resolved reflectivity factor:

$$Z_e = \eta \frac{\lambda^4 10^{18}}{\pi^5 |K_w|^2} \quad (2)$$

where $|K_W|$ is set to 0.75 (representative for water at 10°C at W band).

[19] The CPR provides one vertical profile of η (and thus Z_e) for each integration time interval T_I = 0.16 s, corresponding to subsatellite motion of 1.09 km (±10 m depending on latitude). The actual integration of pulses lasts for 96.8% of T_I (±0.1% depending on latitude). The resulting horizontal resolution after integration and including latitudinal dependence is between 1.3 and 1.4 km cross-track and between 1.7 and 1.8 km along track (defined at the 6dB point of the two-way resulting weighting function,

Table 1). The CPR acquires 125 samples per profile, one every ~240 m. Since the spacecraft altitude varies with position along the orbit, the radar timing parameters are adjusted based on a lookup table to keep the Earth troposphere inside the 30 km science data window. This window includes both the surface return in its lower portion of the profile and a 5–10 km cloud free region in the upper portion of the profile occurring in the stratosphere. The former is a useful reference for detection of precipitation and the latter allows for accurate noise floor estimation and noise subtraction to achieve the required minimum detectable reflectivity (or sensitivity).

3.2. Calibration

[20] Absolute calibration requires precise knowledge of r, λ, G_{rec}, Ω, Δ, P_{rec}, and P_t. Prelaunch calibration parameters were obtained either directly from laboratory measurements or by analysis of experiment data. An equivalent 2 dBZ radiometric calibration accuracy of the CPR is expected over the life of the mission. On orbit, the transmit power P_t and receiver gain G_{rec} are routinely measured via internal calibration channels of the radar. Both have remained remarkably stable since launch. The receiver gain has remained within <0.1 dB over the first 18 months of operation, and external calibration indicates the orbital average of P_t also has remained stable to significantly better than 0.4 dB since launch. Instantaneous measures of P_t, however, are affected by orbit dependent fluctuations that vary by 0.7 dB peak to peak.

[21] CPR end-to-end system calibration is evaluated using measured backscatter off the ocean surface. This method, referred to as external calibration, is widely used in many downward-looking airborne and spaceborne radar systems [*Li et al.*, 2005; *Durden et al.*, 1994; *Tanelli et al.*, 2006; *Schroeder et al.*, 1982]. The method relies on measuring the backscatter off the ocean surface at an angle at which the sensitivity to wind is minimal. Over the 12 months between August 2006 and August 2007, the CloudSat spacecraft has performed several calibration maneuvers steering the CPR antenna 10° to the left or right of the track over preselected cloud-free oceanic areas. This exercise is performed monthly and has verified that the absolute calibration of the CPR is well within the required 2 dB requirement [*Tanelli et al.*, 2008].

[22] The on-orbit performance of the radar has also been independently verified by comparison with measurements obtained from several airborne programs since launch. The example of Figure 4 is from one flight of the airborne cloud radar system (CRS) [*Li et al.*, 2004] flown over a precipitating convective system (middle panel) that developed off the east coast of Georgia, USA as part of the CALIPSO-CloudSat Validation Experiment (CCVEX http://suborbital.nasa.gov/media/) campaign. The CRS was flown on NASA's ER2 and the ground track of the aircraft was matched to the ground track of CloudSat (upper cross section). Analysis shows the reflectivity of the two radars agree within 2dB (lower panel) except in the region of heavy precipitation where multiple scattering in the CloudSat footprint becomes an issue [e.g., *Haynes et al.*, 2008; *Battaglia et al.*, 2006] or where the cloud is small enough to be missed by the CRS but detected within the larger CloudSat footprint.
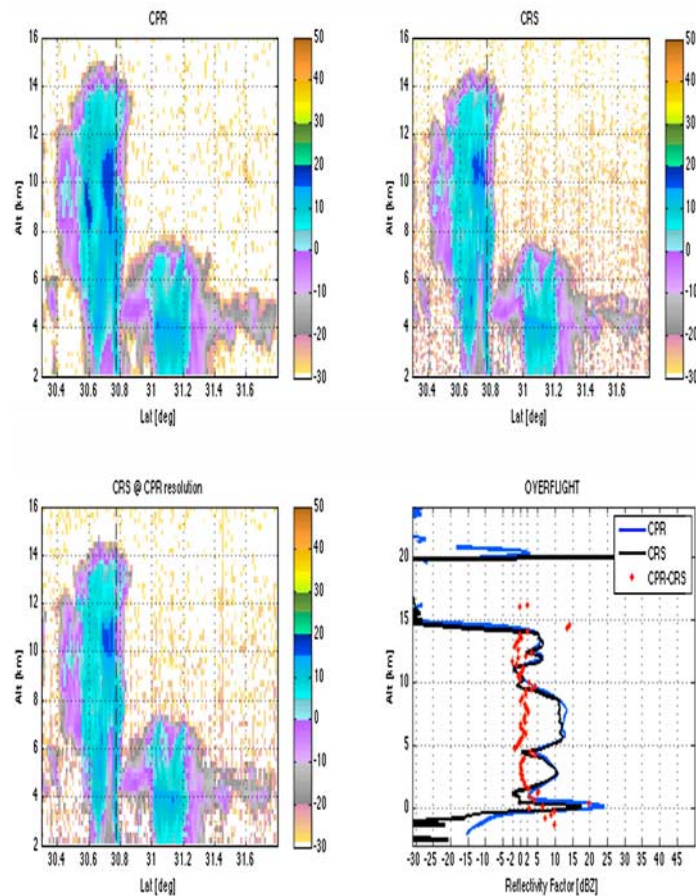
Figure 4. A portion of a CloudSat orbit and the matched underflight of the NASA ER2 over a tropical thunderstorm. (a) The CPR cross section, (b) the matched cloud radar system (CRS) cross section, and (c) the CRS cross section degraded to the resolution of the CPR. (d) The profile along the dashed line corresponding to a precise time of overlap between the CRS and CPR. The difference between the CRS and CPR is less than 2BZ (red profile) except as noted in the text.

3.3. Minimum Detectable Signal

[23] As mentioned, Z_{min} was an important instrument design parameter. This minimum factor is defined as the cloud reflectivity factor Z_e, which, after averaging and noise subtraction, yields a power equal to the noise power standard deviation. Z_{min} is therefore determined by the equivalent noise floor and by the number of transmitted pulses. The noise floor ultimately depends on the radiometric temperature of the observed scene at 94 GHz. Figure 5 is a map of Z_{min} derived from the observations collected during October, 2006. The CPR single-beam Z_{min} varies by about one dBZ over the globe due to radiometric differences between cold scenes (such as clear air over ice at nighttime) and hot scenes (clear air over dry land desert during daytime). On the basis of the current calibration, the minimum detectable reflectivity ranges from −29.9 dBZ to −30.9 dBZ. Seasonal changes in temperature, land cover, and sea ice affect the distribution of Z_{min}. The latitudinal banding evident in Figure 5 is a result of changes to the number of transmitted pulses which varies according to the orbital shape and thus is not geophysical.

[24] Given that the radiometric signal of the background determines the minimum detectable signal, then this minimal signal contains radiometric information about the observed background scene. This radiometric information, by construction, is matched precisely to the footprint of the radar and can be presented in the usual way as a brightness
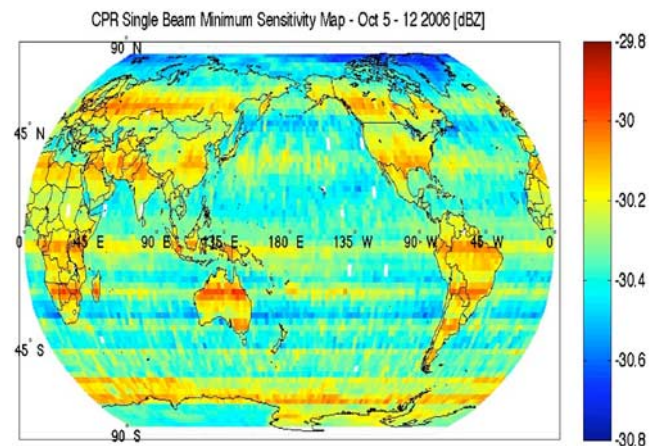

Figure 5. The minimum reflectivity determined from characteristic noise levels of the CPR (refer to text for discussion).
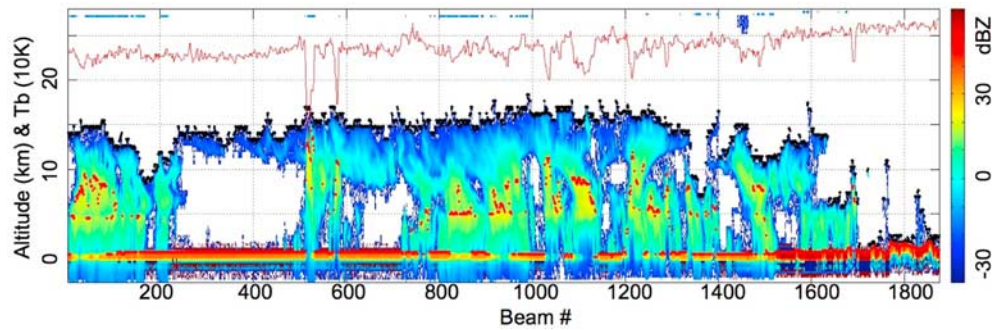
STEPHENS ET AL.: CLOUDSAT EARLY RESULTS

Figure 6. The along track radiometric temperature of a tropical storm observed by CloudSat (upper curve) and the corresponding CPR reflectivity profiles (lower, colored contours). The red points superimposed on these reflectivity contours are the height at which the observed radiometric temperature matches the ECMWF temperature.

Table 2. Summary of Products

| Standard Product ID	Description	Principal Inputs and Product Size/Day
1A-Aux	Auxiliary data for navigation altitude assignments, raw CPR data	Digital Elevation maps, space craft ephemeris
1B-CPR	Calibrated radar reflectivities	Radar power, calibration factors 347 MB
2B-GEOPROF	Cloud geometric profile – includes as mask (with confidence measure), reflectivity (significant echoes), (gas) attenuation correction, and MODIS mask	1B-CPR, MODIS mask product. 498 MB
2B-GEOPROF-LIDAR	Includes the fraction of a CPR bin filled with clouds as determined by lidar.	2B-GEOPROF + CALIPSO LIDAR 290 MB
2B-CLDCLASS	8 classes of cloud type, including precipitation identification and likelihood of mixed phase conditions	Radar and other data (temperature, MODIS) from the constellation 282 MB A version to include lidar information is under development (2B-CLDCLASS-LIDAR)t
2B-TAU	Cloud optical depth by layer, also effective radius (column)	2B-GEOPROF and MODIS radiances
2B-CWC-RO, 2B-CW-RVOD	Cloud liquid water content (2B-LWC) Cloud Ice water content (2B-IWC)	A radar only (RO) version that uses 2B-GEOPROF and temperature, (5291 MB) and a radar-optical depth version (RVOD) that combines 2B-GEOPROF and 2B-TAU
2B-FLXHR	Atmospheric radiative fluxes and heating rates	2B-GEOPROF, 2B-TAU, 2B-CWC - 1516 MB. A version to include lidar information is under development (2B-FLXHR-LIDAR)t
Auxiliary Data Products		
MODIS-AUX	MODIS radiances and cloud mask product	Radiances (MOD02) from 23 of the MODIS channels and mask (MOD35) subsetted to 3X5 km about CloudSat.
AN-MODIS	MODIS 1B radiances and 2B products subsetted abut the CPR footprint	The data from MODIS-AUX plus selected products from MOD04-05-06 and -07
AN-SSF	CERES single satellite footprint (SDSF) products matched to CPR	Surface and TOA fluxes from the CERES flash flux product
AN-state variables	Subset of ECMWF along track of various forecast model state variables, energy fluxes, etc.,	The subsetting details are currently under study to constrain data volume sizes
Enhanced Products		
2B-rain Precipitation (liquid)	Precipitation incidence, Surface rainrate, profiles of liquid water content in precipitation	2B-GEOPROF, ECMWF-AUX wind speed and SST, and AMSR-AUX radiances
2B-snow Precipitation (solid)	Precipitation incidence, profiles of snow particle size distribution parameters and snowfall rate	2B-GEOPROF, ECMWF-AUX temperature
2B-CC-ICE	Profiles of number concentration, particle size and ice water content.	2B-GEOPOF, 2B-TAU, CALIPSO lidar, MODIS radiances
AN-AMSRE	AMSR radiances and level 2 products matched to the CPR	AMSR-E level 2A radiances, rainfall, CWV,LWP SST and wind speed from the AMSR-E ocean product
AN-PR	TRMM PR reflectivities and rainfall products matched to CPR reflectivity and rainfall products.	TRMM 1C21 reflectivities, rainfall products 2A21 and 2A25 and CloudSat's 2B-GEOPROF and new rainfall products
Special Products		
TC-CloudSat	CloudSat profile data mapped into a cyclindrical coordinate relative to storm center location (radial distance from storm, azimuthal direction). MODIS and AMSR-E products matched to CloudSat and also placed into this coordinate system.	2b-GEOPROF mask, CPR reflectivities, AMR-E wind, water vapor, LWP, rain rates, MODIS cloud top temp, pressure, height and brightness temp, and "best track" storm center, max wind speed, SST, and selected NoGAPS fields
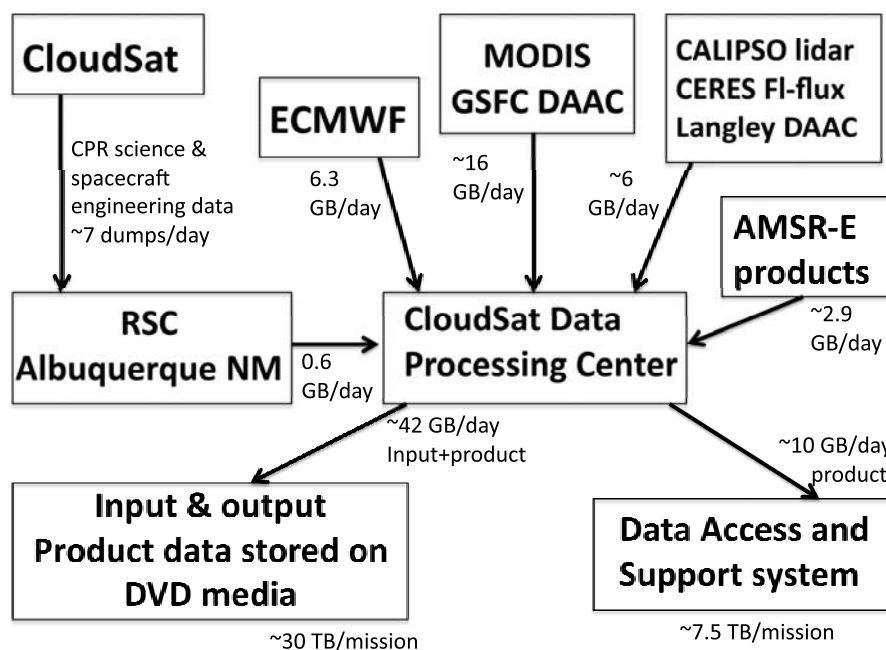
Figure 7. A schematic of the data flow through the CloudSat data processing center (DPC) and data rates associated with production of the CloudSat products at the DPC.

temperature. An example of this radiometric information presented in the form of preliminary, calibrated W band brightness temperatures is presented in Figure 6 showing the microwave emission from tropical cyclone Ewinar contrasted against the matched, along-track CPR reflectivity data. The estimated NEΔT of a single footprint is approximately derives from an estimated resolution of 0.05 dB in measurements of the noise floor at the receiver output. Accurate absolute calibration for this measurement has not yet been performed and at this time there are no plans to produce this radiometric information as part of the standard level 1B product.

4. Science Data Products and Validation

[25] The standard data products (Table 2) are produced at the DPC and are available via http://www.cloudsat.cira. colostate.edu/dpcstatusQL.php. The data processing activity thus far has primarily concentrated on production of Level 1 and Level 2 products as summarized in Table 2. An indication of the daily, total rate of flow of data through the DPC, with inputs, outputs, and indicated volumes, is provided in Figure 7. Although the total output of Level 1 and 2 data products, including the ancillary products noted in Table 2, total approximately 42 GB/d, the volume of the most elementary of the products, namely the 1B-CPR and 2B-GEOPROF is produced at a rate of only 116 and 189 Mb/d, respectively. This is small in comparison to many other satellite data sources. Table 3 provides a summary of the performance of the data ground segment in collecting and processing data. As of October, 2007 the amount of data collected and processed, out of the ideal possible of 100%, has far exceeded both requirement and expectation.

[26] The 1B-CPR product provides calibrated sensor-level information expressed in terms of the reflectivity

quantities discussed in section 3. The second main product is the 2B-GEOPROF [*Mace et al.*, 2007] derived from the 1B-CPR. The 2B-GEOPROF identifies the location of hydrometeors in the Earth's atmosphere using a cloud-masking algorithm, provides estimates of the atmospheric gaseous attenuation of the radar signal, provides cloud identification information derived from Aqua MODIS data for use in data analysis and cloud-property retrieval algorithms, and assigns the radar reflection values to the detected clouds. Although Figure 1 is an example of the quick-look data, these types of data shown are available from the 2B-GEOPROF product. All other level 2 products derive from the 2B-GEOPROF product. At this time all standard level 2 products listed in Table 2 have been processed and released. All results presented below are based on the latest R04 release of data.

[27] Examples of two other standard data products are provided in Figures 8 and 9. Figure 8 shows the 2006/2007 December–January–February (DJF) seasonal frequency of occurrence of zonally averaged cloudiness derived from the 2B- GEOPROF-LIDAR (Figure 8a) which is a merger of the 2B-GEOPROF and the CALIPSO lidar feature mask data [*Mace et al.*, 2008]. Figure 8 also shows the equivalent distribution derived from the 2B-GEOPROF (Figure 8b) as

Table 3. Summary of Data Processing Performance as of October 2007

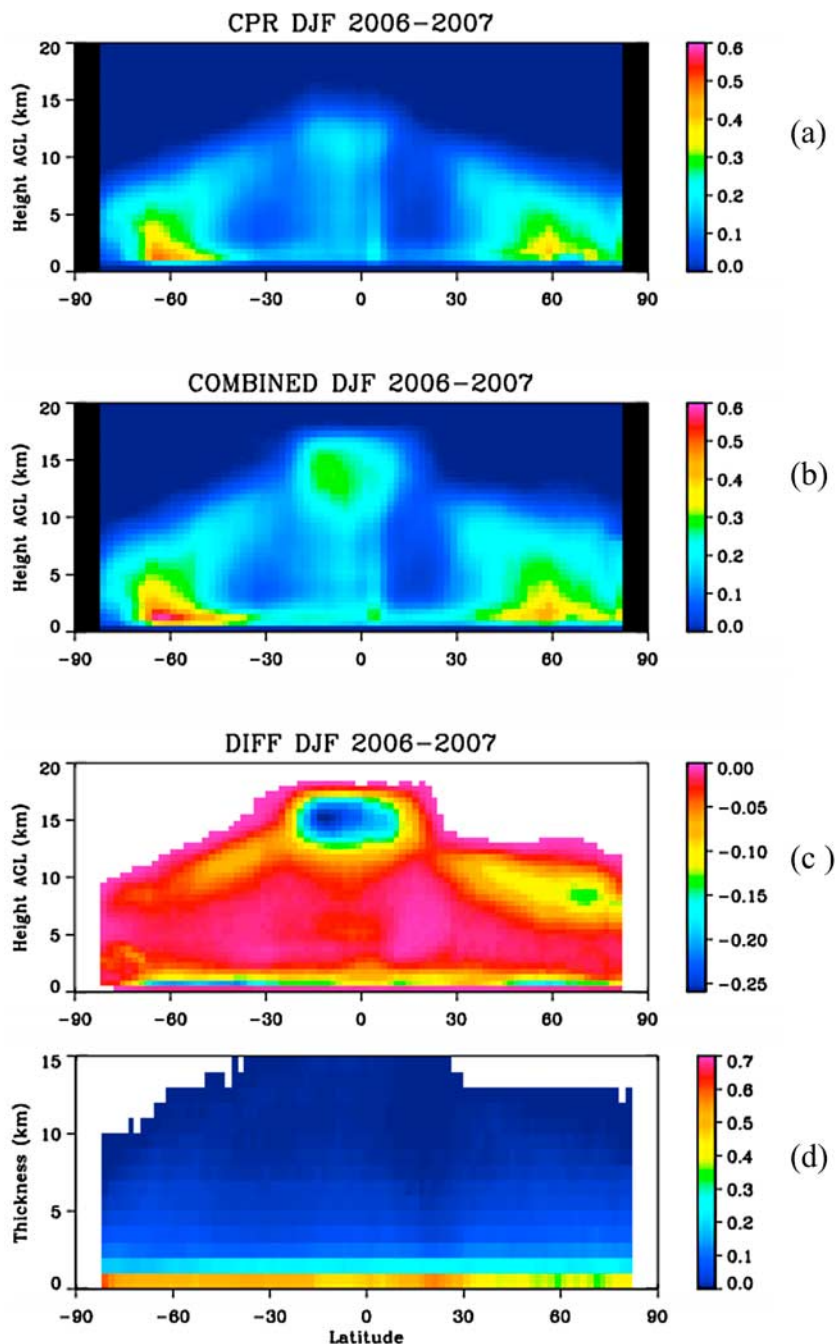|	Requirement	Performance
CloudSat Project	85%	96.93%
Cloud Profiling Radar	96%	99.17%
Spacecraft	96%	98.52%
Research Testing Development and Evaluation Support Center	94%	99.21%
Cooperative Institute for Research in the Atmosphere	98%	100%

Figure 8. (a) The zonally averaged frequency of occurrence of Clouds as detected by the CPR and (b) as determined by the combined 2B_GEOPORF-LIDAR product. (c) The difference between Figures 8b and 8a highlighting the clouds missed by the radar, and (d) the zonally accumulated frequency of occurrence of cloud thickness.

well as the difference between these two products (Figure 8c). Reasons for the discrepancies highlighted in Figure 8c are understood [*Mace et al.*, 2008]. Because the CPR surface returns contaminates the first two or three bins (below about ∼720 m) above the surface, small (e.g., fair weather) cumulus and low cloud with tops below 1 km are under represented in the CloudSat data. Another factor is the sensitivity of radar that impacts the detectability of some cumulus, nondrizzling stratocumulus, and warm altocumulus composed of small water droplets [e.g., *Sassen and Khvorostyanov*, 2007], as well

as optically thin, high cirrus. Figure 8d presents the frequency of occurrence of cloud thickness, a quantity not previously available from satellite observations and information unique to CloudSat and the 2B-GEOPROF and 2B- GEOPROF-LIDAR products. The higher frequency exemplified in the bottom 2 km of Figure 8d emphasizes that cloud thicknesses are most frequently in the range from 2 km and less and that the deep convection in the tropics (thickness exceeding 10 km), for example, occurs less than 5% of the time.
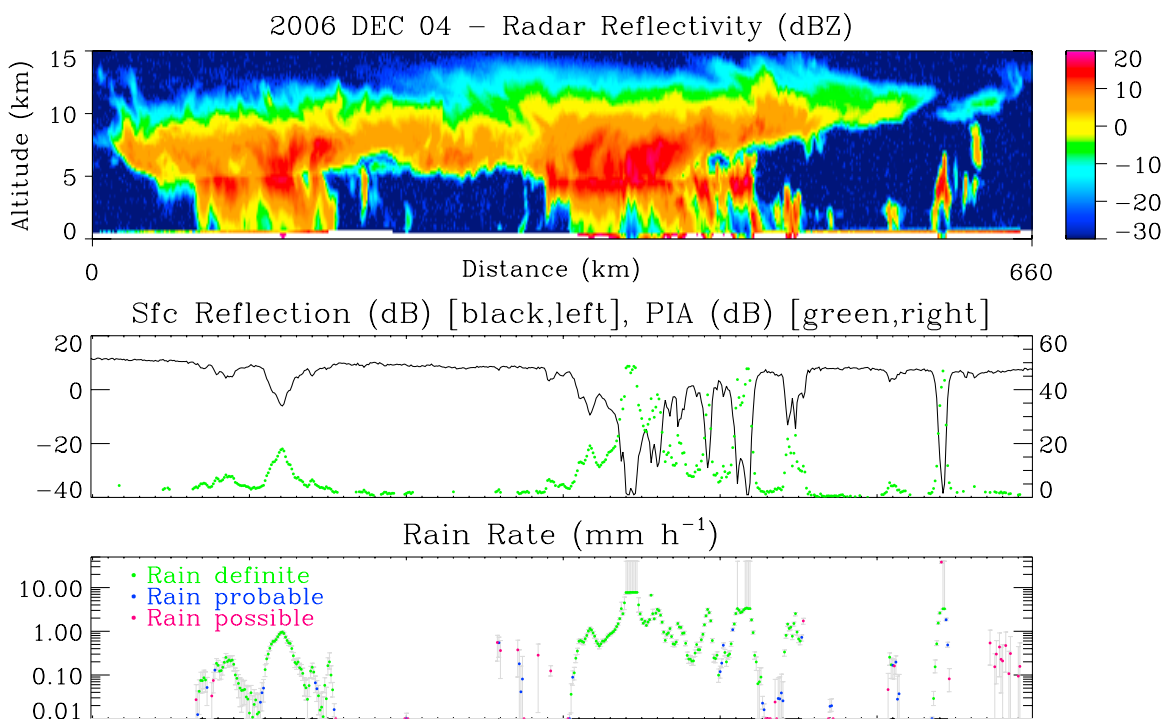
Figure 9. (top) An example of the CPR cross section through a precipitating system over the ocean, also illustrating (middle) the surface reflectivity and derived path attenuation and (bottom) the rain categorization.

[28] In addition to the standard products, a number of other auxiliary and experimental products have been developed to support scientific analyses of the data. Some of the experimental products (notably precipitation and ice microphysics) are to become part of the standard data product suite during the extended mission phase that begins in mid-2008. A number of the ancillary products noted in Table 2 are also in various stages of development and their release is to be announced.

[29] Validation of products is an ongoing activity that will continue through the life of the mission and beyond. Validation occurs on many levels, such as through evaluation of the physical basis of algorithms [e.g., *Heymsfield et al.*, 2008], through intercomparison with similar products derived from different observations and underlying physics [e.g., *Wu et al.*, 2008], and through direct ground-truth validation (e.g., Figure 6). Validation activities are highly leveraged, taking advantage of sustained long-term systematic observations and related validation efforts at selected ground-based sites supported by the DOE-ARM program, selected NASA and ARM airborne science campaigns as noted with respect to Figure 6, and various national and international university and government activities supported through the current Science Team.

5. Selected Results

5.1. Precipitation

[30] The power backscattered to the CPR by any given range-resolved volume of atmosphere is highly sensitive to the presence of precipitation due both to scattering by precipitation within the volume and to attenuation by precipitation within and between the volume and the CPR. This sensitivity is utilized in the construction of the CloudSat precipitation products. These products are in various stages of development. One of the products [*Haynes et al.*, 2008], based on the estimation of radar attenuation, is comparatively mature and the evaluation of it is ongoing.

[31] The attenuation of the CPR is a result of a combination of absorption by gases such as O_2 and H_2O, absorption by cloud droplets, and the absorption and scattering by precipitation sized particles. Isolating the two-way path integrated attenuation (PIA) of the entire atmospheric column at the frequency of the CPR provides a very sensitive way of determining the presence of precipitation within the column [*Haynes and Stephens*, 2007; *Haynes et al.*, 2008]. Over ocean surfaces, this PIA can be determined to better than 2 dB, based on estimating of the ocean reflectivity under precipitation. The PIA derived in this way provides a very sensitive indication of precipitation with an estimated minimum sensitivity of approximately 0.02–0.05 mm/h [*Haynes et al.*, 2008].

[32] Detection of precipitation over oceans from the estimated PIA is based on determining the equivalent unattenuated radar reflectivity adjacent to the ocean surface. The larger the value of this reflectivity in the range bins just above the ocean surface, the more likely it is that precipitation has occurred at the surface itself. Threshold values of this near-surface reflectivity thus establish the likelihood of precipitation. For example, an unattenuated near-surface reflectivity of 0 dBZ or higher is practically certain to be associated with significant rain, corresponding to rain rates of about 0.03 mm h^{-1} and greater. To produce the same precipitation rate in pure snow, scattering simulations suggest only −5 dBZ is required, so this threshold is adjusted
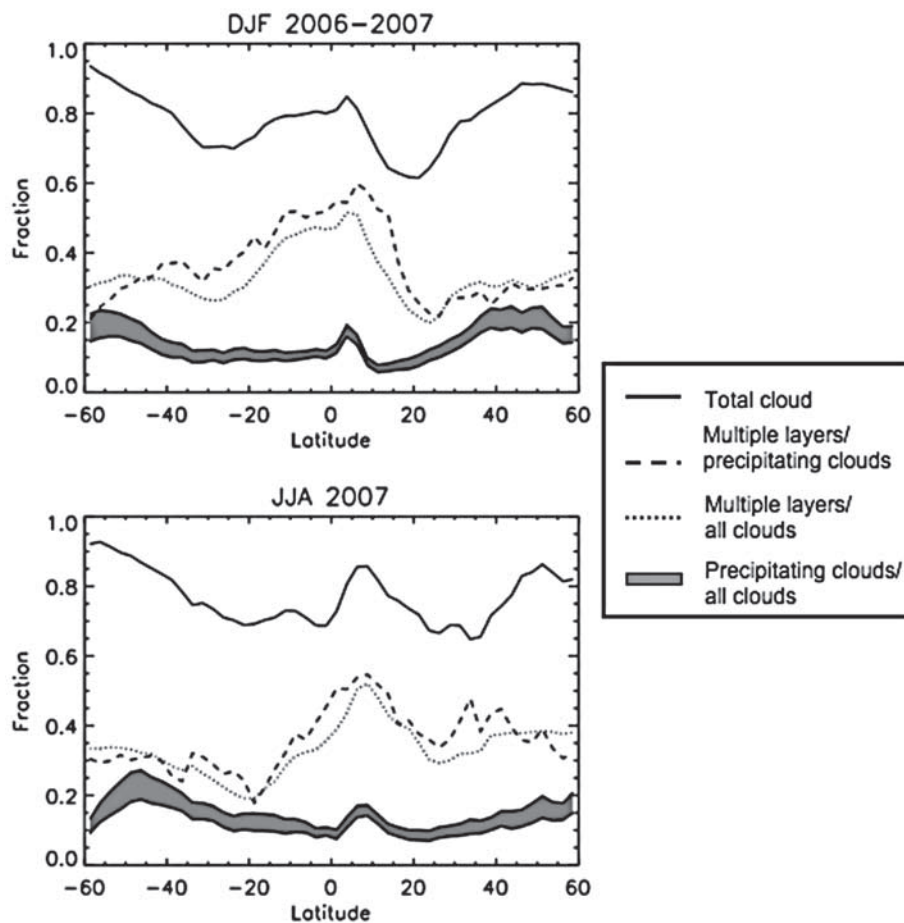
Figure 10. The zonally averaged (ocean only) total cloud cover and the fraction of this total cloudiness producing precipitation that in all likelihood reaches the surface (shaded line, refer to text for explanation). The middle sets of curves are the proportion of all clouds and all precipitating clouds that are part of a multilayered cloud system.

accordingly when the numerical weather analysis operational temperature profile indicates the entire atmosphere is colder than 0° C. For both rain and snow, a reflectivity less than -15 dB is highly unlikely to be associated with falling precipitation including light drizzle [*Matrosov et al.*, 2004], and this criterion is used to define the "no rain" category with certainty. Intermediate reflectivity values between these limits establish increasing likelihoods of precipitation occurrence. These intermediate regimes, as introduced by *Haynes et al.* [2008], are the "rain probable" regime for this low-level reflectivity between -7.5 dBZ and 0 dBZ and the "rain possible" regime for reflectivity between -7.5 dBZ and -15 dBZ.

[33] Figure 9 illustrates the PIA approach showing a portion of one granule of data of the CPR through a wide-scale precipitating convective system over the ocean (Figure 9, top), the measured ocean surface reflectivity (Figure 9, middle) together with the deduced PIA. Figure 9 (bottom) provides the rain classification regimes and the rain rate derived from the PIA.

[34] Both precipitation incidence as described above and precipitation amount are produced in a format that facilitates simple matching of this information to all other available products. One example of the benefit of this matched information is highlighted in the aerosol-indirect effect study of *Lebsock et al.* [2008]. Another example is presented in Figure 10 showing the zonal, seasonally averaged cloud frequency of occurrence derived from the 2B-GEO-PROF-LIDAR data originally binned into 2×2 degree latitude-longitude grid boxes accumulated over the two seasons shown. The zonal average shown applies to ocean only and can be interpreted as the zonal, seasonally averaged cloud fraction. The lower set of curves with shading are the zonal average of the fraction of the detected clouds in each grid box that are deemed to be definitely precipitating according to the criteria defined above (lower curve) and the fraction of clouds that include both the definite precipitation plus the probable precipitation category of clouds (upper curve). The global means of these data indicate that approximately 11% of clouds detected over the global oceans produce precipitation that in all likelihood reaches the ocean surface. This fraction is not constant globally varying with latitude in a way that appears to mirror large-scale circulation features. For example, the fraction of precipitating clouds increases in regions where large-scale, low-level convergence of moisture is expected, notably in the region of the ITCZ and the baroclinic zones of the winter midlatitudes.
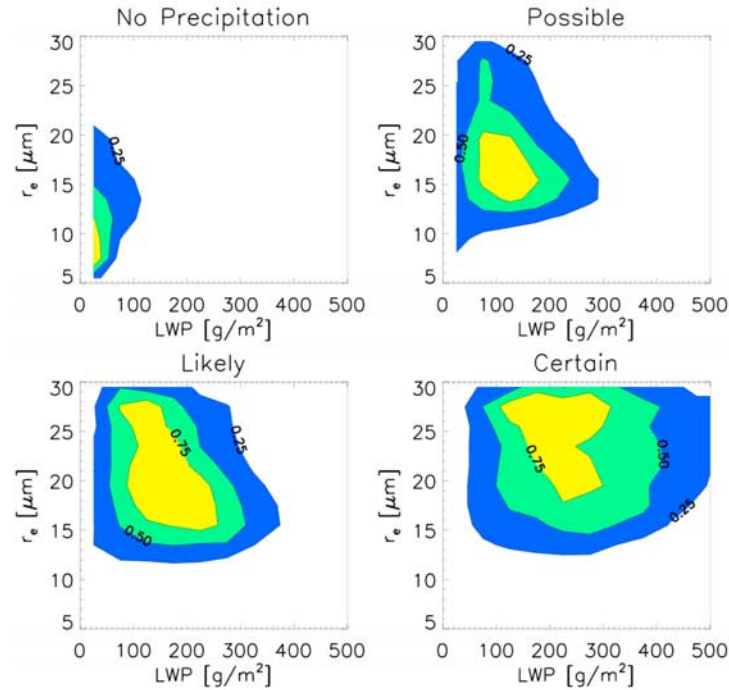
Figure 11. The joint distributions of cloud liquid water path and effective radius classified into the four precipitation categories derived from matched CloudSat CPR observations.

[35] The middle set of curves in Figure 10 show the fraction of all clouds detected that are part of a multilayered system and the fraction of all precipitating clouds that are also part of multilayered cloud systems. A high percentage of the precipitating clouds of the tropics are multilayered, principally composed of high cloud layers over precipitating clouds of varying depths.

5.2. Warm Clouds

[36] Changes to the cloud albedo figure prominently in a number of important cloud-climate feedback concepts [*Stephens*, 2005]. Albedo changes related to aerosol changes also establish the indirect effects of aerosol on climate. Hence, it is of some importance to understand the factors that influence the albedo of clouds in order to set the context for understanding possible aerosol influences.

[37] The amount of sunlight reflected from clouds is determined largely (although not entirely) by the scaled optical depth of clouds of the form τ (1-g), where τ is the cloud optical depth and g is the asymmetry parameter. Since the latter quantity is more or less fixed and known a priori for water clouds, then the reflection of sunlight from such clouds can be thought of as governed primarily by τ. Using the relation of *Stephens* [1978], then

$$\tau = \frac{3}{2\rho}\frac{W}{r_e} \qquad (3)$$

where W is the liquid water path of (warm) clouds and r_e is the effective radius. Thus the cloud albedo is function of W and r_e. Satellite measurements of reflected sunlight in selected regions of the solar spectrum, as provided by MODIS for example, provide a way of estimating both τ and r_e and thus W [*Stephens and Kummerow*, 2007].

[38] The Twomey effect [*Twomey*, 1977] appears in (3) via the reduction of r_e that occurs with enhanced levels of CCN associated with enhanced concentrations of aerosol assuming fixed values of W. Although the idea of the Twomey effect is simple enough, it has proven to be much more difficult than expected to determine if the effect is widespread globally and thus has an observable, global consequence on sunlight reflected by the planet. The difficulty of such assessment, in part, stems from the many factors that potentially contribute to observed variations in cloud albedo. In particular, the liquid water path of clouds W also varies with changing aerosol amount [e.g., *Lebsock et al.*, 2008; *Albrecht*, 1989].

[39] According to (3) there are two important dependences that need to be isolated in studying the albedo of clouds and ultimately in inferring possible influences of aerosol on this albedo. The first is the dependence of optical depth on particle size (r_e) and the second is the dependence of optical depth (and hence albedo) on W. The latter dependence has typically been overlooked in satellite-based studies of the indirect effect, yet we will show its influence on cloud albedo is significant and in some instances dominant. As we will show, the relation between cloud albedo, W and particle size is also made complicated by the presence of precipitation.

[40] The combination of CloudSat observations matched to MODIS and CERES (AN-MODIS, AN-SSF, Table 2) provides a unique opportunity to characterize the properties of W and r_e jointly and subsequently relate them to the cloud albedo. Figure 11 shows the joint distribution of the MODIS-derived cloud water path W and effective radius r_e for oceanic, warm clouds where the matched CPR precipitation classification has been applied to these data. The results show how warm precipitating clouds tend to be
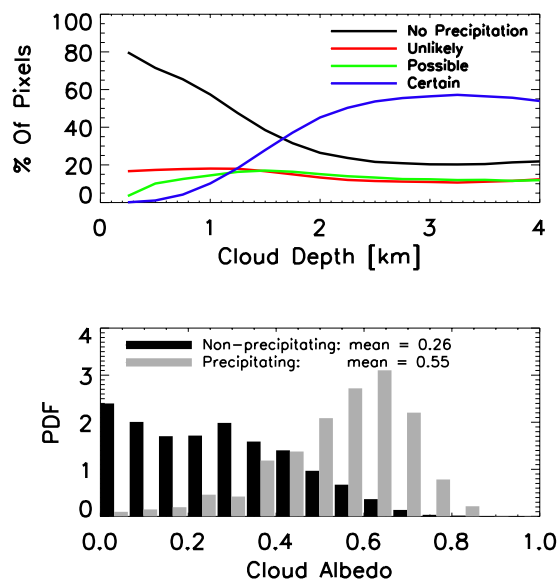
Figure 12. (a) The percentage of individual CPR column profiles that contain the four different classes of rain as a function of cloud depth. (b) The probability distribution of cloud albedo for nonprecipitating and precipitating clouds based on matched CERES and CPR data.

both wetter (larger W) and composed of larger particles (i.e., larger r_e) than nonprecipitating clouds. The probability of precipitation increases significantly with cloud depth (Figure 12a) and thus precipitating clouds are geometrically deeper than nonprecipitating clouds. Increased water paths of precipitating clouds also contribute to an increased optical depth. The increase in particle size, however, is a contrary effect that acts to decrease the optical depth. The combination of these two compensating factors, however, do not cancel, and the optical depths of warm precipitating clouds tend to be significantly larger than those of nonprecipitating clouds. As a consequence, these geometrically deeper, wetter precipitating clouds reflect substantially more sunlight than nonprecipitating warm clouds (Figure 12b).

5.3. Cold Clouds

[41] Another important goal of the mission is to provide quantitative information about the ice contents of global clouds. The motivation for this goal has been addressed in a number of previous papers that call out the importance of cloud ice content on climate feedbacks [e.g., *Stephens et al.*, 1990; *Waliser et al.*, 2008]. The need for such information is further underscored by the lack of agreement between current climate models (*Stephens et al.* [2002] and Figure 13 below) and the lack of an authoritative global-ice database to test these models.

[42] The CloudSat 2B-CWC-RO data product provides an estimate of ice water content [*Austin et al.*, 2008], and the ice water path (IWP) derived from this product is presented in Figure 13a in the form of global and annual averaged IWP. These products include both precipitating and nonprecipitating ice and this, in itself adds ambiguity when comparing to global models [e.g., *Waliser et al.*, 2008]. The IWP is shown for each of the cloud types defined by the 2B-CLDCLASS product, and the data are

further grouped into "convective" (cumulus and deep convection) and "nonconvective" (all other types) cloud categories as way of separating clouds with non precipitating ice from clouds with precipitating ice. The uncertainties shown correspond to the estimated, systematic uncertainties derived from analysis as described in more detail by *Austin et al.* [2008].

[43] The nonconvective IWP, the convective IWP, and the sum of the two are compared in Figure 13b to the global and annually averaged IWP derived from several coupled-climate models where the model data are taken from the 1970–1994 period of the 20th century GCM simulations contributed to the IPCC 4th Assessment Report (20c3m scenario). Any conclusions drawn from this direct comparison between model and observation should viewed with some caution given the way models segregate clouds into large-scale and convective types and then segregate ice into precipitating ice and nonprecipitation ice. Most convective schemes used by models do not include ice specifically, and it is thus tempting to consider the nonconvective ice IWP of CloudSat as a closer proxy to the modeled ice. However, most convective schemes contain some form of detrained ice indirectly, and it is reasonable to consider some of the observed convective ice content should also be included in the comparison. Although these ambiguities have to be born in mind, it appears that the IWPs of most models are significantly less than observed especially if we consider that the appropriate observed ice path for comparison lies somewhere between the CloudSat nonconvective ice and total ice amounts shown. The interpretation of the CloudSat IWP and model IWP will continue to be a topic of future research and is discussed further by *Waliser et al.* [2008].

5.4. Radiative Effects of Clouds

[44] Another of the original motivating factors for the CloudSat mission was the desire to provide the necessary observations that could better address the question: to what extent do clouds radiatively heat or cool the atmosphere relative to the clear skies on the global scale? Addressing this question is important for many reasons as noted by *Stephens* [2005] and exemplified in the study of *Stephens and Ellis* [2008].

[45] The vertical structure of clouds largely determines the sign of the net atmospheric heating by clouds and it has not been possible to determine this atmospheric heating from previous cloud information without gross assumptions about this structure. The CloudSat 2B-FLXHR product incorporates the available observations of cloud vertical structure and derived water contents [*L'Ecuyer et al.*, 2008] in calculations of the vertical profiles of radiative fluxes (and thus heating rates) in cloudy columns. Analysis of 12 months of the 2B-FLXHR product, as shown in Figure 14a, directly addresses the question posed above. Figure 14a provides the estimated contribution of clouds to the column atmospheric radiative heating (relative to clear skies) for different latitudinal regions and for the entire globe. Figure 14b is an equivalent presentation of the data based on an experimental version of the 2B-FLXHR that adds lidar cloud information. The details of how these undetected (by the CPR) clouds are included in the 2B-FLXHR product are described by *L'Ecuyer et al.* [2008]. Figures 14c and 14d present these cloud radiative heating contributions for three ranges of cloud top height.
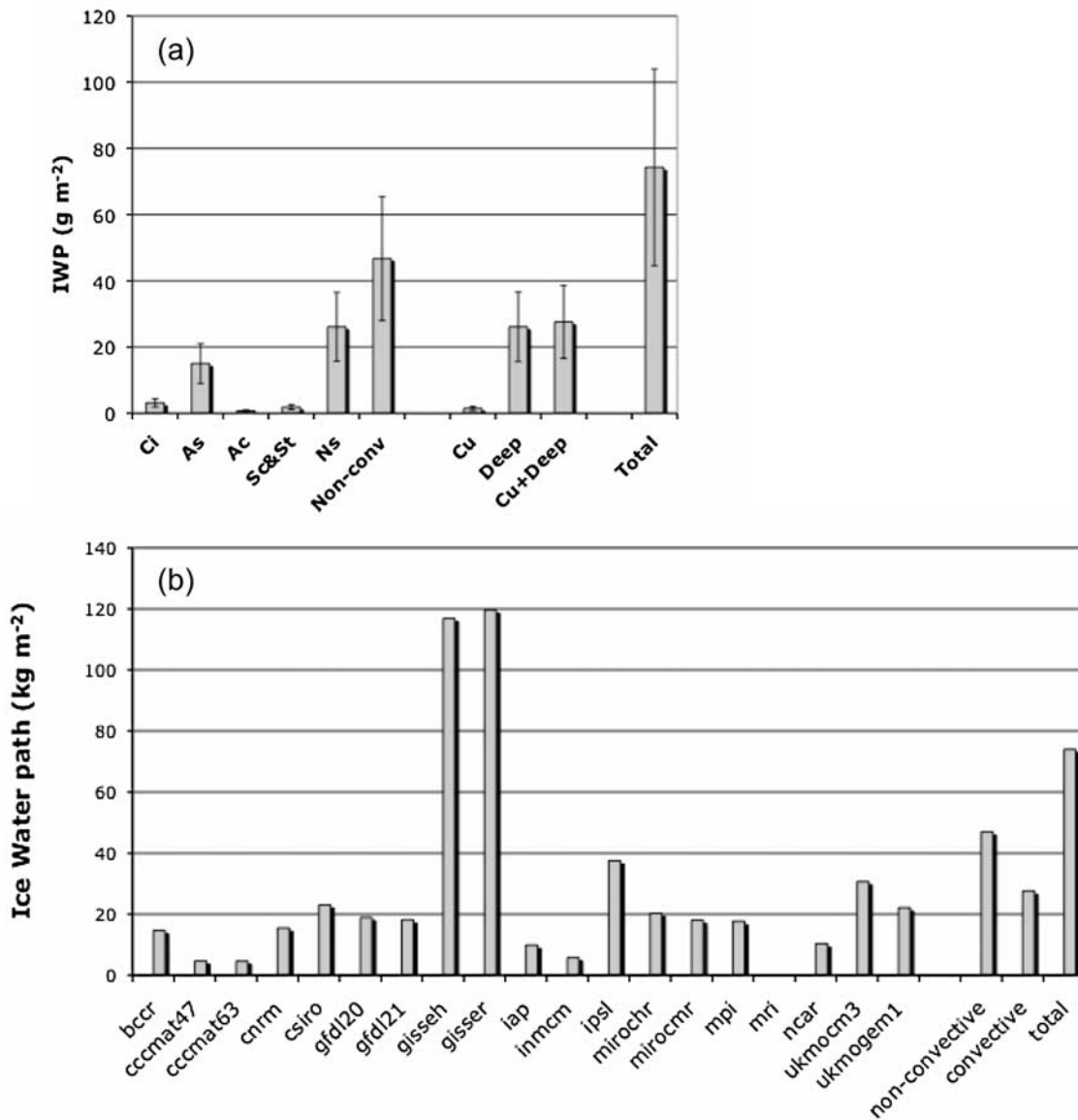
Figure 13. (a) Global mean ice water path calculated from Release 4 (R04) of the CloudSat 2B-CWC-RO product over the period 2006-12-01 to 2007-11-30. Ice water path is assigned to cloud types using the 2B-CLDCLASS product. "Convective" cloud refers to the sum of 2B-CLDCLASS cumulus and deep convection types; "nonconvective" includes the remaining types. Error bars indicate the estimated systematic uncertainties. (b) The global mean ice water path derived from 19 Intergovernmental Panel on Climate Change (IPCC) climate models from the 1970–1994 period of the 20th century GCM simulations contributed to the IPCC 4th Assessment Report (20c3m scenario) compared to the CloudSat observations of nonconvective, convective, and total repeated from Figure 13a.

[46] According to Figure 14, clouds heat the global mean atmospheric column by about 10 Wm^{-2}. Although this heating appears to be contributed almost equally by solar and infrared absorption, the latter contribution varies significantly with latitude and is influenced by the predominant cloud structures of the different regions. The absorption of infrared radiation by high clouds, for example, dominates in the lower latitudes giving rise to an infrared heating by clouds at low latitudes. The emission of infrared radiation from lower clouds at higher latitudes contributes to an enhanced column cooling at these latitudes.

[47] The differences between the respective radar and radar-lidar results serve as a gross indication of the effects on the radiation budget of those clouds missed by the radar alone. These differences reveal themselves particularly in the lower latitudes where some of the thin cirrus missed by the radar contributes to the infrared heating, as well as in the polar regions where some low clouds undetected by the radar adds to the column cooling. Some differences in midlatitudes are also evident where the low-lying clouds undersampled by the radar results in an underrepresentation of the cooling contribution by these clouds.
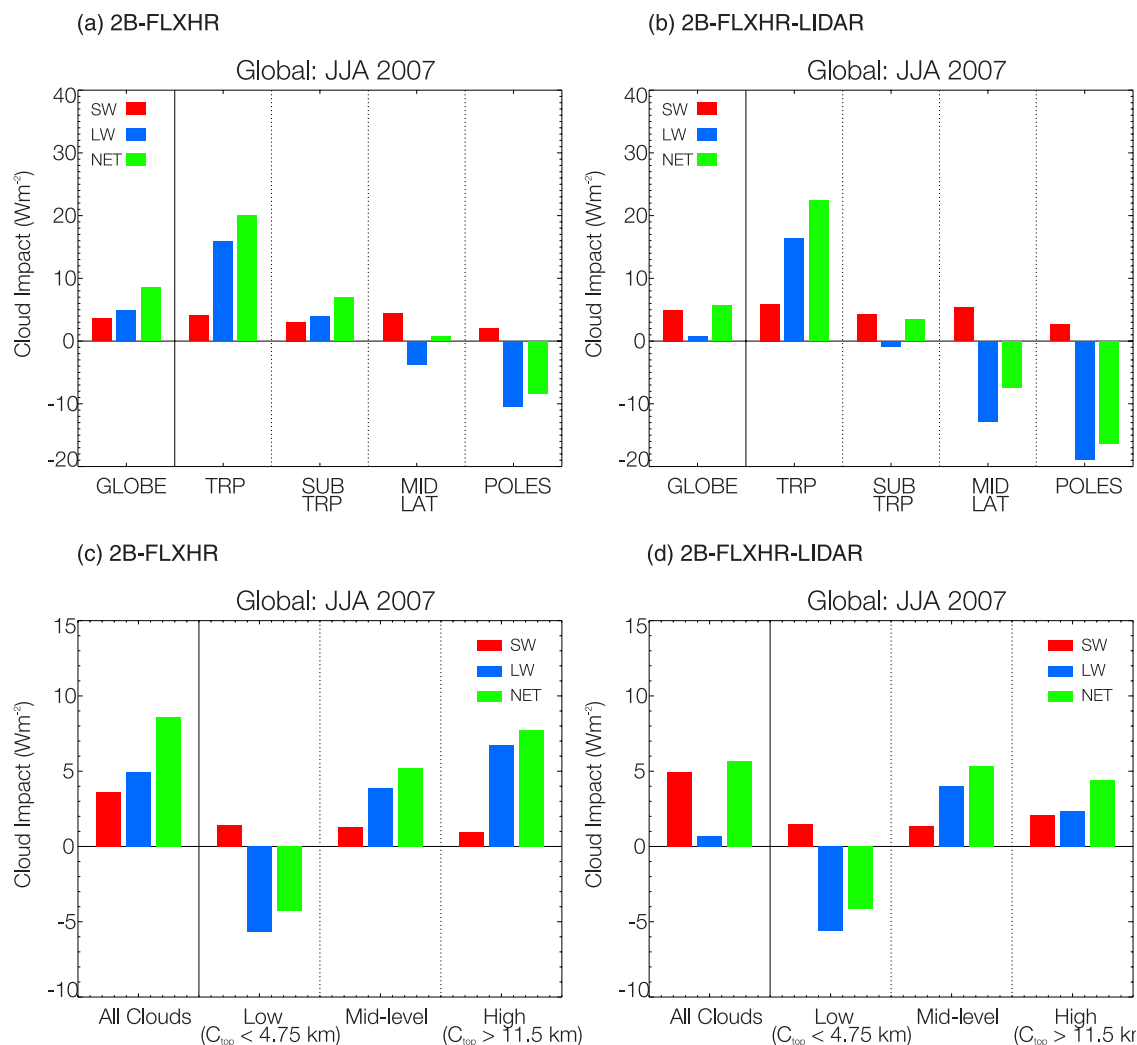
Figure 14. The vertically integrated contribution of clouds to the atmospheric column radiative heating for the June−July−August season as derived from the CloudSat flux-heating rate products indicated.

5.5. Comparison to Models

[48] The recent study of *Kay et al.* [2008] illustrated how changes to Arctic clouds during the summer of 2007 may have significantly impacted the summer sea ice loss of 2007. Given also that climate change simulations point to a larger warming in the polar regions, then an evaluation of modeled arctic cloudiness is likely to be an important contribution in determining the ultimate credibility of climate change projections.

[49] Evaluation of the global depictions of clouds in models using the new observations available from the A-Train should lead to improved parameterizations of cloud processes; this is another important CloudSat mission science goal. Model evaluation activities are ongoing and are developed around the use of the CPR simulator [e.g., *Haynes et al.*, 2007; *Bodas-Salcedo et al.*, 2008].

[50] The use of a radar simulator coupled to a climate model is also illustrated in the results shown in Figure 15, showing observed and simulated profiles of radar reflectivity in arctic clouds. A developmental version of NCAR's community atmosphere model ("CAM-dev") was coupled to the radar simulator to produce the radar reflectivity information shown on Figure 15. CAM-dev is CAM3 [*Collins et al.*, 2006] with modifications to the deep-convection scheme and a new two-moment stratiform microphysics scheme [*Morrison and Gettelman*, 2008; *Gettelman et al.*, 2008]. Three years of CAM-dev instantaneous dBZ values saved at 6 hourly intervals are compared to the CloudSat reflectivity observations accumulated between June 2006 and December 2007. The comparisons shown are for the cloudiest season for two regions in the Arctic: Fall (SON) in the Beaufort Sea and Winter (DJF) in the Barents Sea. The diurnal sampling of the observations and the model output are not the same, but this is considered not significant given there is not a strong diurnal cycle in Arctic cloudiness. Comparisons below 0.96 km are also not shown because of surface clutter effects on the CPR observations.

[51] The comparisons presented in Figure 15 are in the form of normalized contoured frequency by altitude diagrams (CFADs). Vertical cloud fraction profiles are also shown. These profiles correspond to cloud fractions derived for volumes defined as "cloudy" if the reflectivity lies between −30 dBZ and 10 dBZ. The normalized CFAD
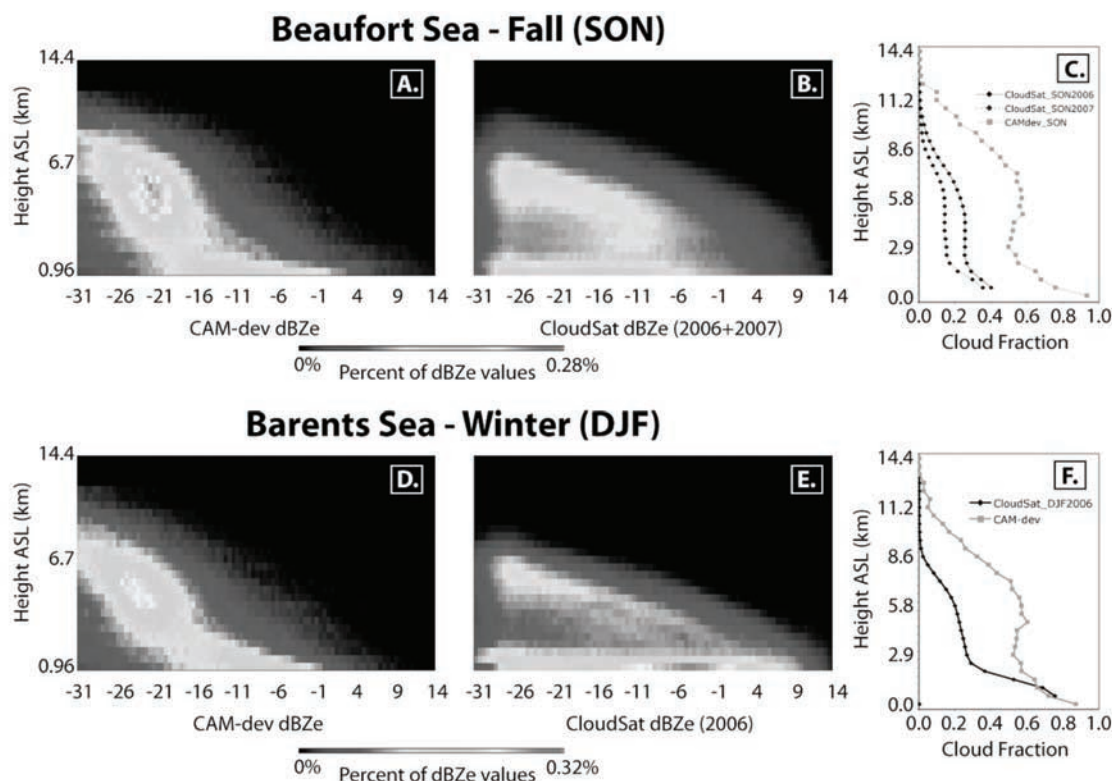
Figure 15. CloudSat versus Climate Model (CAM-dev) representations of vertical structures of arctic clouds. The comparisons are in the form of (a, b, d and e) contoured frequency by altitude diagrams for the Beaufort Sea (September–October–November) and the Barents Sea winter (December–January–February) and also in the form of (c and f) the vertical distribution of cloud fraction.

diagrams for both the climate model and the observations suggest two main populations of clouds: a low cloud population below approximately 2 km characterized by wide a range of dBZ values, and a mid-high cloud population whose dBZ values decrease with height and are less variable than the low-cloud reflectivity distribution. The reflectivity of the low clouds in the models varies much less than observed. CAM-dev misses clouds with dBZ values less than −21 dBZ in both the Barents and the Beaufort Sea. In the Barents Sea, CAM-dev also misses low clouds with larger dBZ values (dBZ > 0) which is indicative of snowfall during this season. Examination of the cloud fraction profiles also reveals significant differences between model and observations. The CAM-dev has substantially more clouds than CloudSat, especially above the boundary layer, and the vertical structure of cloudiness in the model is similar for the Beaufort and the Barents Sea, whereas the CloudSat data suggest differences in the cloud fraction vertical profile presumably associated with distinct differences in circulation features between these regions. Research that examines the implication of these comparisons on the parameterizations of arctic cloudiness is ongoing.

6. Summary

[52] This paper reports on the early mission performance of the radar and other major aspects of the CloudSat mission. The cloud profiling radar (CPR) has been operating since 2 June 2006, and since that time only 10 h of data have been lost due

to planned maneuvers and 200 h due to infrequent instrument malfunctions. The radar has also been remarkably stable over this period, its calibration has been verified to be within the 2dB requirement, and it operates with a minimum detectable signal varying between −30 to −31 dBZ, depending on the scene being observed.

[53] A number of products have been developed using these radar data as principal inputs, and new products are being developed that merge other A-Train sensor data, notably the lidar observations of CALIPSO. These new data provide unique, global views of the vertical structure of clouds and key information about how clouds affect the atmosphere. Among the new findings drawn from these observations are as follows:

[54] 1. The ability of CloudSat to jointly observe clouds and precipitation provides new insights on the way water cycles through the atmosphere. These observations reveal that approximately 11% of clouds detected over the global oceans produce precipitation that in all likelihood reaches the surface. This fraction varies significantly with latitude in a way that mirrors large-scale circulation features.

[55] 2. Joint CloudSat and MODIS observations of warm clouds clearly indicates that warm precipitating clouds are both wetter and composed of larger particles than nonprecipitating clouds. The frequency of precipitation increases significantly with increasing cloud depth, and the increased depth and water path of precipitating clouds leads to increased optical depths and substantially more

sunlight reflected from precipitating clouds compared to than nonprecipitating warm clouds.

[56] 3. The global ice water path IWP predicted from most climate models appear to be significantly less than the global inferences of the ice water path from CloudSat observations. However, the comparison between model and observations must be viewed with some caution at this time due to the way models parameterize clouds and convection. The interpretation of the CloudSat IWP versus the model IWP will continue to be a topic of future research. The results of the IWP comparison presented serve as a generally caution in the interpretation of comparisons between models and A-train observations. In an effort to address potential ambiguities and other difficulties that arise with such comparisons, radar and lidar instrument simulators have been developed and are currently being coupled to global models.

[57] 4. CloudSat observations indicate that clouds radiatively heat the global mean atmospheric column (relative to clear skies) by about 10 Wm^{-2}. Although this heating appears to be contributed almost equally by solar and infrared absorption (Figures 14a and 14b), the latter contribution varies significantly with latitude being influenced by the predominant cloud structures of the different region in questions.

References

Albrecht, B. (1989), Aerosol, cloud microphysics, and fractional cloudiness, *Science*, 245, 1227–1230, doi:10.1126/science.245.4923.1227.

Austin, R. J., A. J. Heymsfield, and G. L. Stephens (2008), Retrievals of ice cloud microphysical parameters using the CloudSat millimeter wave radar and temperature, *J. Geophys. Res.*, doi:10.1029/2008JD010049, in press.

Battaglia, A., M. O. Ajewole, and C. Simmer (2006), Evaluation of radar multiple scattering effects in CloudSat configuration, *Atmos. Chem. Phys.*, 7, 1719–1730.

Bodas-Salcedo, A., M. J. Webb, M. E. Brooks, M. A. Ringer, K. D. Williams, S. F. Milton, and D. R. Wilson (2008), Evaluating cloud systems in the Met Office global forecast model using simulated CloudSat radar reflectivities, *J. Geophys. Res.*, doi:10.1029/2007JD009620, in press.

Collins, W. D., et al. (2006), The Community Climate System Model Version 3 (CCSM3), *J. Clim.*, 19, 2122–2143, doi:10.1175/JCLI3761.1.

Deschamps, P. Y., F. M. Breon, M. Leroy, A. Podaire, A. Bricaud, J. C. Buriez, and G. Seze (1994), The POLDER mission: Instrument characteristics and scientific objectives, *IEEE Trans. Geosci. Remote Sens.*, 32, 598–615.

Durden, S. L., E. Im, F. K. Li, W. Ricketts, A. Tanner, and W. Wilson (1994), ARMAR: An airborne rain-mapping radar, *J. Atmos. Oceanic Technol.*, 11, 727–737, doi:10.1175/1520-0426(1994)011<0727:AAARMR>2.0.CO;2.

Gettelman, A., H. Morrison, and S. J. Ghan (2008), A new two-moment bulk cloud microphysics scheme in the Community Atmospheric Model (CAM3), Part II: Single-column and global results, *J. Clim.*, 21, 3660–3679, doi:10.1175/2008JCLI2116.1.

Haynes, J., and G. L. Stephens (2007), Tropical ocean cloudiness and the incidence of precipitation: Early results from CloudSat, *Geophys. Res. Lett.*, 34, L09811, doi:10.1029/2007GL029335.

Haynes, J., R. T. Marchand, Z. Luo, A. Bodas-Salcedo, and G. L. Stephens (2007), A multipurpose radar simulation package: QuickBeam, *Bull. Am. Meteorol. Soc.*, 88, 1723–1727, doi:10.1175/BAMS-88-11-1723.

Haynes, J., T. L'Ecuyer, G. Stephens, S. Miller, C. Mitrescu, and S. Tanelli (2008), Rainfall retrieval over the ocean with spaceborne W-band radar, *J. Geophys. Res.*, doi:10.1029/2008JD009973, in press.

Heymsfield, A. J., et al. (2008), Testing IWC retrieval methods using radar and ancillary measurements with in-situ data, *J. Appl. Meteorol. Climatol.*, 47, 135–163.

Im, E., C. Wu, and S. L. Durden (2005), Cloud profiling radar for the CloudSat mission, paper presented at Radar Conference, IEEE, Piscataway, N. J.

Kay, J. E., T. L'Ecuyer, G. L. Stephens, A. Gettelman, and C. O'Dell (2008), The contribution of cloud and radiation anomalies to the 2007 Arctic sea ice extent, *Geophys. Res. Lett.*, 35, L08503, doi:10.1029/2008GL033451.

L'Ecuyer, T. S., N. B. Wood, T. Haladay, G. L. Stephens, and P. W. Stackhouse Jr. (2008), Impact of clouds on the atmospheric heating based on the R04 CloudSat fluxes and heating rates data set, *J. Geophys. Res.*, doi:10.1029/2008JD009951, in press.

Lebsock, M., G. L. Stephens, and C. Kummerow (2008), Multisensor observations of aerosol effects on warm clouds, *J. Geophys. Res.*, 113, D15205, doi:10.1029/2008JD009876.

Li, L., G. M. Heymsfield, P. E. Racette, L. Tian, and E. Zenker (2004), The 94 GHz Cloud Radar System on a NASA ER-2 Aircraft, *J. Atmos. Oceanic Technol.*, 21, 1378–1388, doi:10.1175/1520-0426(2004)021<1378:AGCRSO>2.0.CO;2.

Li, L., et al. (2005), Measurements of ocean surface backscattering using an airborne 94-GHz cloud radar - implication for calibration of airborne and spaceborne W-band radars, *J. Atmos. Oceanic Technol.*, 22, 1033–1045, doi:10.1175/JTECH1722.1.

Mace, G. G., R. Marchand, Q. Zhang, and G. L. Stephens (2007), Global hydrometeor occurrence as observed by CloudSat: Initial observations from summer 2006, *Geophys. Res. Lett.*, 34, L09808, doi:10.1029/2006GL029017.

Mace, G. G., Q. Zhang, M. Vaughn, R. Marchand, G. Stephens, C. Trepte, and D. Winker (2008), A description of hydrometeor layer occurrence statistics derived from the first year of merged Cloudsat and Calypso data, *J. Geophys. Res.*, doi:10.1029/2007JD009755, in press.

Matrosov, S. Y., T. Uttal, and D. A. Hazen (2004), Evaluation of radar reflectivity-based estimates of water content in stratiform marine clouds, *J. Appl. Meteorol.*, 43, 405–419, doi:10.1175/1520-0450(2004)043<0405:EORREO>2.0.CO;2.

Miller, S. D., and G. L. Stephens (2001), CloudSat instrument requirements as determined from ECMWF forecasts of global cloudiness, *J. Geophys. Res.*, 106, 17,713–17,733, doi:10.1029/2000JD900645.

Mitrescu, C., S. Miller, G. Hawkins, T. L'Ecuyer, J. Turk, P. Partain, and G. Stephens (2008), Near real time applications of CloudSat data, *J. Appl. Meteorol.*, 47, 1982–1994.

Morrison, H., and A. Gettelman (2008), A new two-moment bulk stratiform cloud microphysics scheme in the Community Atmospheric Model (CAM3), Part I: Description and Numerical Tests, *J. Clim.*, 21, 3642–3659, doi:10.1175/2008JCLI2105.1.

Posselt, D., G. L. Stephens, and M. Miller (2007), CloudSat: Adding a new dimension to a classical view of extratropical cyclones, *Bull. Am. Meteorol. Soc.*, 89, 599–609.

Sassen, K., and V. I. Khvorostyanov (2007), Microphysical and radiative properties of mixed phase altocumulus: A model evaluation of glaciation effects, *Atmos. Res.*, 84, 390–398, doi:10.1016/j.atmosres.2005.08.017.

Schroeder, L. C., et al. (1982), The relationship between wind vector and normalized radar cross section used to derived SEASAT-A Satellite Scatterometer winds, *J. Geophys. Res.*, 87(C5), 3318–3337, doi:10.1029/JC087iC05p03318.

Stephens, G. L. (1978), Radiation profiles in extended water clouds: II. Parameterization schemes, *J. Atmos. Sci.*, 35, 2123–2132, doi:10.1175/1520-0469(1978)035<2123:RPIEWC>2.0.CO;2.

Stephens, G. L. (2005), Cloud feedbacks in the climate system: A critical review, *J. Clim.*, 18, 237–273, doi:10.1175/JCLI-3243.1.

Stephens, G. L., and T. D. Ellis (2008), Global- scale controls of precipitation efficiency in global warming GCM experiments, *J. Clim.*, in press.

Stephens, G. L., and J. Haynes (2007), Near global observations of the warm rain auto-conversion process, *Geophys. Res. Lett.*, 34, L20805, doi:10.1029/2007GL030259.

Stephens, G. L., and C. Kummerow (2007), The remote sensing of clouds and precipitation from space: A review, *J. Atmos. Sci.*, 64, 3742–3765, doi:10.1175/2006JAS2375.1.

Stephens, G. L., S.-C. Tsay, P. W. Stackhouse Jr., and P. J. Flatau (1990), The relevance of the microphysical and radiative properties of cirrus clouds to climate and climate feedback, *J. Atmos. Sci.*, 47, 1742–1753, doi:10.1175/1520-0469(1990)047<1742:TROTMA>2.0.CO;2.

Stephens, G. L., et al. (2002), The CloudSat mission and the A-TRAIN: A new dimension to space-based observations of clouds and precipitation, *Bull. Am. Meteorol. Soc.*, 83, 1771–1790, doi:10.1175/BAMS-83-12-1771.

Tanelli, S., S. L. Durden, and E. Im (2006), Simultaneous measurements of Ku- and Ka-band sea surface cross-sections by airborne radar, *IEEE Geosci. Remote Sens. Lett.*, 3(3), 359–363, doi:10.1109/LGRS.2006.872929.

Tanelli, S., S. L. Durden, E. Im, K. Pak, D. Reinke, P. Partain, J. Haynes, and R. Marchand (2008), CloudSat's cloud profiling radar after 1 year in orbit: Performance, external calibration, and processing, *IEEE Trans. Geosci. Remote Sens.*, in press.

Twomey, S. (1977), The influence of pollution on the shortwave albedo of clouds, *J. Atmos. Sci.*, 34, 1149–1152, doi:10.1175/1520-0469(1977)034<1149:TIOPOT>2.0.CO;2.

Waliser, D., et al. (2008), Cloud Ice: A climate model challenge with signs and expectations of progress, *J. Geophys. Res.*, doi:10.1029/2008JD010015, in press.

Winker, D. M., W. H. Hunt, and M. J. McGill (2007), Initial performance assessment of CALIOP, *Geophys. Res. Lett.*, *34*, L19803, doi:10.1029/2007GL030135.

Wu, D. L., et al. (2008), Comparison of global cloud ice from MLS, CloudSat and correlative data sets, *J. Geophys. Res.*, doi:10.1029/2008JD009946, in press.

————————————

R. Austin, J. Haynes, M. Lebsock, T. L'Ecuyer, G. L. Stephens, and K. Suzuki, Department of Atmospheric Sciences, Colorado State University, Fort Collins, CO 80523, USA. (Austin@atmos.colostate.edu; Haynes@atmos.colostate.edu; lebsock@atmos.colostate.edu; Tristan@atmos.colostate.edu; stephens@atmos.colostate.edu; kenta@atmos.colostate.edu)

S. Durden, E. Im, M. Rokey, S. Tanelli, D. G. Vane, D. Waliser, and D. Wu, Jet Propulsion Laboratory, California Institute of Technology, 4800 Oak Grove Drive, Pasadena, CA 91109, USA. (stephen.durden@jpl.nasa.gov; eastwood.im@jpl.nasa.gov; mark.rokey@jpl.nasa.gov; simone.tanelli@jpl.nasa.gov; dvane@jpl.nasa.gov; duane.waliser@jpl.nasa.gov; Dong.L.Wu@jpl.nasa.gov)

A. Gettelman and J. Kay, National Center for Atmospheric Research, Boulder, CO 80305, USA. (andrew@ucar.edu; jenkay@cgd.ucar.edu)

G. G. Mace, Department of Meteorology, University of Utah, Salt Lake City, UT 84112, USA. (mace@met.utah.edu)

R. Marchand, Joint Institute for the Study of the Atmosphere and Ocean, University of Washington, Seattle, WA 98195, USA. (rojmarch@u.washington.edu)

P. Partain, Science Technology Corporation, MetSat, Fort Collins, CO 80323, USA. (partain@cira.colostate.edu)

D. Reinke, CIRA, Colorado State University, Fort Collins, CO 80523, USA. (reinke@cira.colostate.edu)

Z. Wang, Department of Atmospheric Science, University of Wyoming, Laramie, WY 82071, USA. (zwang@uwyo.edu)